Hindawi
Advances in Civil Engineering
Volume 2019, Article ID 1509719, 15 pages
https://doi.org/10.1155/2019/1509719

Research Article

A Multicomponent Particle Model and Linear Fitting Calibration Method for Heterogeneous Rocks

Qifeng Guo,[1,2] **Ying Zhang**,[1,2] **Xun Xi**,[1,2] **Xu Wu**,[1,2] **and Meifeng Cai**[1,2]

[1]*School of Civil and Resource Engineering, University of Science and Technology Beijing, Beijing 100083, China*
[2]*Beijing Key Laboratory of Urban Underground Space Engineering, University of Science and Technology Beijing, Beijing 100083, China*

Correspondence should be addressed to Qifeng Guo; guoqifeng@ustb.edu.cn

Received 29 November 2018; Revised 24 February 2019; Accepted 4 March 2019; Published 1 April 2019

Academic Editor: Robert Černý

Deformation and failure of rock are very important to underground space engineering. In this paper, a new three-dimensional multicomponent bonded-particle model is developed for heterogeneous rocks. Granite samples from the Sanshandao Gold Mine are first analyzed using a microscope. Cylindrical and disc models consisting of four minerals (i.e., plagioclase, potash feldspar, quartz, and biotite) are built to simulate the behavior of the granite under compressive and tensile tests. To improve the calibration efficiency, a new method for determining the microparameters of minerals is proposed. Uniaxial compression, triaxial compression, and Brazilian tests are carried out in the lab. The failure pattern and stress-strain curves are obtained from numerical simulations and verified with those observed in the experiments. Furthermore, the Mohr–Coulomb and Hoek–Brown strength parameters are obtained and compared with the experimental results. The multicomponent particle model is shown to well reproduce the behavior of granite under the compressive and tensile tests. The multicomponent bonded-particle model significantly improves the accuracy of three parameters: the ratio of tensile strength to uniaxial compressive strength, the friction angle, and the parameter m_i of the Hoek–Brown criterion. The linear fitting calibration method provides a fast and efficient way to determine the microparameters of particles in heterogeneous rocks.

1. Introduction

Due to the rapidly increasing demands for city space, more and more underground constructions and infrastructures are designed and built in the world. The deformation and failure of rock are important to underground space engineering. Rock is normally considered as a heterogeneous geomaterial consisting of multiple minerals. The failure of rock is characterized by complicated micromechanical processes, including the nucleation, growth, and coalescence of microcracks. The behavior of rock deformation and failure has a large influence on the stability of geotechnical engineering projects. Landslides, tunnel collapse, and rock burst greatly threaten the lives of people and engineering safety [1, 2]. Therefore, a thorough investigation of the mechanisms of rock deformation and failure behavior is well justified.

The deformation, damage accumulation, and crack patterns of rocks are commonly examined by tensile and compressive tests [3, 4, 5, 6]. Over the past two decades, numerical methods have been developed to provide increasing insight into the mechanical behaviors of rock samples. Lan et al. [7] developed a grain-based model considering grain-scale heterogeneity to simulate the microstructure of brittle rock by UDEC and found that crack initiation stress is controlled by the microscale geometric heterogeneity. Particle-based models, which were originally developed to simulate the behavior of cohesive frictional materials (e.g., soils and sands), are now often used for rock modeling. Compared with element- or mesh-based models (e.g., FEM, BEM, lattice model, and FDEM), particle-based models can reproduce the micromechanical behaviors of rock, such as microcrack nucleation, growth, and coalescence. Moreover, complex constitutive relationships are

replaced with simple particle contact logic in particle-based models. Therefore, many researchers have resorted to particle-based models in simulating the deformation and failure behavior of rocks under tensile and compressive tests at both meso- and microscales. Potyondy et al. simulated the macromechanical parameters of Lac du Bonnet granite by using the bonded-particle model (BPM) [8]. Fakhimi et al. [9] employed the BPM to model biaxial compressive tests of notched sandstone and found that the model could reproduce the damage zone of samples as experimental results. Zhang and Wong [10–12] captured microcrack initiation, growth, and coalescence by using the BPM, with the simulation results being in good agreement with the experimental results. Zhang et al. [13] employed parallel bonded-particle models to simulate crack coalescence between two nonparallel flaws. Ji et al. [14] developed a new method to model the crack closure behavior of rock under compression by introducing preexisting opened microcracks with notional surfaces and gap in PFC. Kulatilake et al. [15] used the BPM to investigate the effect of joints on the uniaxial compressive strength (UCS) of samples. Park and Song [16] carried out direct shear tests by using the BPM and found that the simulated shear failure behavior is consistent with that observed in experiments. Poulsen and Adhikary [17] employed the BPM to simulate compressive tests of coal samples and obtained the stiffness and strength of the coal samples. More studies have proved that the BPM can reproduce the behavior of samples under mechanical tests and yield Young's modulus, Poisson's ratio, and UCS of rock. However, these models do not consider the multiple minerals in rock, and the existing models face three difficulties: (1) the ratio of tensile strength (TS) to UCS of rock, i.e., TS/UCS, yielded is larger than the real value; (2) the friction angle is smaller than the real value; and (3) the parameter m_i of the Hoek–Brown (HB) failure criterion is smaller than the real value.

For the particle-based modeling methodology, an extensive calibration based on experimentally measured macroscale properties is required to determine the contact parameters, which are very cumbersome and complex. Most studies commonly used the trial-and-error method to determine the contact parameters. The trial-and-error method is as follows: by keeping other parameters constant, investigating the effect of a single parameter or a combination of parameters on simulation results, comparing the macromechanical parameters with the experimental results, and then repeating the above steps again and again, the parameters that best predict the observed macroscale response can be obtained. To improve the efficiency of parameter determination, some researchers have resorted to using some new algorithms, e.g., the global optimization package SNOBFIT, orthogonal design or BP neural network. Zhou et al. [18] built a nonlinear BP neural network model for connecting macromechanical parameters to contact parameters. Liu et al. [19] used the orthogonal design method to determine the contact parameters and discussed the relationship between macromechanical parameters and contact parameters by a multivariate variance analysis. Wu and Xu [20] believed that any parameters in any calibration step will affect each other in terms of the macroresponse and hence developed a program to iteratively calibrate the contact parameters. Vallejos et al. [21, 22] developed an interactive calibration program that can change the contact parameters in real time until the parameters best predicting the macromechanical behavior are obtained. These new methods combining computation and mathematics have improved the efficiency of parameter determination. However, no universally applicable method with which to achieve this determination with high efficiency within a short amount of time exists.

This paper attempts to develop a new multicomponent bonded-particle model (MBPM) for simulating rock micromechanical behavior. Granite samples from the Sanshandao Gold Mine are chosen as the work example. The mineral composition and content of the granite are first scanned and analyzed by using a microscope. Next, the MBPM is built to simulate the behavior of granite under tensile and compressive tests. A new calibration method for determining the microparameters of particles representing different minerals is then proposed. The effect of multiple minerals on the macromechanical response is considered. Compressive and Brazilian tests are carried out in the lab. Then, compressive and Brazilian tests based on the numerical model are carried out. The failure pattern and stress-strain curves are subsequently obtained from the numerical simulations and verified with the experimental results. Finally, the Mohr–Coulomb and HB strength parameters are obtained and compared with the experimental results.

2. A Multicomponent Bonded-Particle Model

In the traditional BPM model with a single mineral component, the mechanical parameters of uniaxial compression and tensile tests can easily be calibrated, at least in part. However, no matter the combination of normal and tangential bond strengths, the ratio of TS/UCS is always approximately 0.25, which is typically larger than the experimental results. Moreover, the internal friction angle and HB strength parameters m_i are often smaller. This outcome likely occurs because all the particles have the same bond and stiffness parameters; thus, the difference in the strength of various minerals and the coordinated deformation of different minerals under loading cannot be reflected. In this paper, the minerals constituting the rock under observation are considered to build a multiphase BPM.

Some granite samples were taken from the Sanshandao Gold Mine, the mining depth of which exceeds 1000 m. The samples were first scanned by using a microscope to analyze their mineral components. As shown in Figure 1, the mineral composition and content can be described as follows: plagioclase (44%), potash feldspar (20.0%), quartz (32%), and biotite (4%). Based on the content of the four minerals, a MBPM is built by PFC and an in-house script is written in FISH. Figure 2 illustrates the multicomponent particle model, where blue, green, red, and yellow particles represent the plagioclase, potash feldspar, quartz, and biotite, respectively.

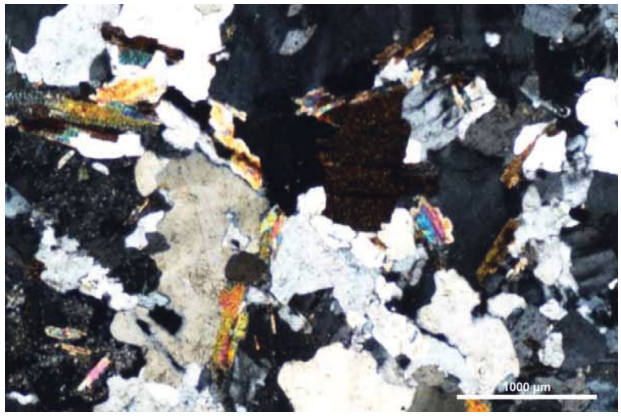

Figure 1: Minerals of the Sanshandao granite under the microscope.

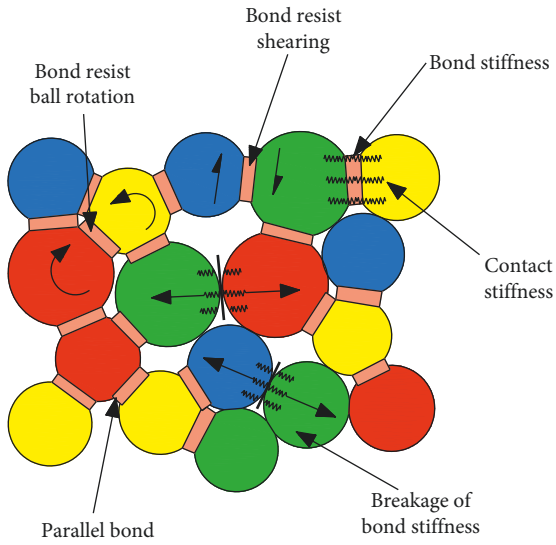

Figure 2: Multicomponent bonded-particle model (MBPM) [10].

As shown in Figure 3(a), a cylindrical MBPM with a 50 mm diameter and 100 mm height is generated to simulate the uniaxial compression tests, which is in agreement with the recommendation on rock sample size by ISRM [23]. The model consists of 3858 spherical particles with varying diameters. The axial load is applied by 2D upper and lower rigid plates with a dimension of 75 mm × 75 mm (length and width, respectively). Figure 3(b) illustrates the MBPM for a triaxial compression test, which is achieved by applying confining pressure to the same model used in the uniaxial compression test. The confining stress is applied by using a cylindrical wall using a servo. Figure 3(c) shows a disc MBPM with a 50 mm diameter and 25 mm height. The model, which is generated to simulate a Brazilian disc split test, contains 3741 spherical particles with varying diameters. The particles are compacted, the internal structure is stable, and the particles are in full contact with each other after the equilibrium state is reached. The models are subjected to a constant displacement load rate until failure. Zhang et al. [11–13, 24] studied the loading rate effect on the simulation results by the particle model and found that the maximum loading rates for the uniaxial compression and Brazilian tests are 0.02 m/s and 0.01 m/s, respectively. To reduce the simulation time, the loading plate speeds used in this paper are the maximum values as the references.

3. Calibration of Micromechanical Parameters

When calibrating the micromechanical parameters for particle flow simulations, most previous studies considered only Young's modulus, Poisson's ratio, and UCS and ignored the damage threshold parameters (e.g., crack initiation stress and crack damage stress) [25, 26, 27, 28]. In this paper, we calibrated the micromechanical parameters to match Young's modulus, Poisson's ratio, UCS, TS, crack initiation stress, crack damage stress, cohesion, and friction angle of the model with respect to those of the rock sample.

Table 1 shows the microparameters in the particle flow simulation, which affect the macrobehaviors of the numerical sample and should be determined via the trial-and-error method. According to previous studies [20, 21, 22], five microparameters, i.e., parallel bond Young's modulus, linearly contacted bonded Young's modulus, ratio of normal to shear stiffness, magnification factor of the strength ratio, and friction angle, have significant effects on the behavior of rock samples. In addition, other microparameters, e.g., radius multiplier, maximum-to-minimum grain diameter ratio, and density, can be determined empirically using the references. As illustrated in Figure 4, the tensile Young's modulus is calibrated by using the Brazilian tests, while the other five microparameters are calibrated by using the uniaxial compressive tests. The final microparameters are used for a triaxial compression test and verified against the experimental results. For the MBPM, the microparameters of particles representing different minerals must be determined, which is much more time-consuming compared to the traditional BPM model. Therefore, we propose a new calibration method with linear fitting that is explained by considering the calibration of the tensile Young's modulus as an example. As shown in Figure 4, the initial values of the parallel bonded modulus of four minerals are determined empirically and then multiplied by n coefficients as the input for the Brazilian tests. The contact parameters between two particles representing two different minerals are simplified as the average values of the contact parameters of them. For example, the contact Young's modulus between the quartz particle and the plagioclase particle is the average value of those in quartz particles and plagioclase particles. According to the n simulation results, the function relationship between the macrotensile Young's modulus and the parallel bond Young's modulus of particles representing individual mineral components can be obtained via the linear fitting method. Finally, the parallel bond Young's modulus can be calculated by substituting the experimental tensile Young's modulus into the function. Note that the other microparameters are constant when determining the parallel bond modulus. The other microparameters are also determined by using this method one by one. This method has the following characteristics: procedural flow, strong pertinence, stability, reliability, and ease of operation. Compared with the trial-

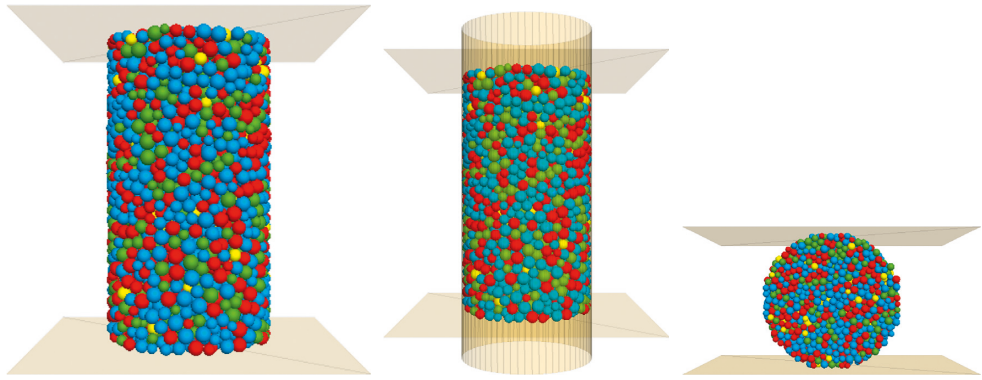

(a) (b) (c)

Figure 3: Numerical models for mechanical tests: (a) uniaxial compression; (b) triaxial compression; (c) Brazilian disc test.

Table 1: Microparameters of the contact bond model and parallel bond model.

Microparameter	Definition	Unit
$\overline{E}^*$	Parallel bond Young's modulus	GPa
E^*	Particle contact Young's modulus	GPa
k_n/k_s	Ratio of particle normal-to-shear stiffness	—
$\overline{k}_n/\overline{k}_s$	Ratio of parallel bond normal-to-shear stiffness	—
$\overline{\sigma}_c$	Parallel bond tensile strength	MPa
$\overline{c}$	Parallel bond cohesion	MPa
$\overline{\phi}$	Friction angle	°
μ	Friction coefficient	—
$\overline{\lambda}$	Radius multiplier	—
R_{min}	Minimum particle radius	Mm
R_{max}/R_{min}	Particle size ratio	—
ρ	Particle bulk density	kg·m^{-3}
n	Porosity	—

and-error calibration method and iterative calibration method, the efficiency of the proposed method is greatly improved.

4. Worked Examples

4.1. Mechanical Experiments on the Sanshandao Granite. The size of the experimental sample and that of the numerical model are the same. No crack is produced when cutting the specimen. Figure 5(a) shows the WEP-600 universal testing machine at the University of Science and Technology Beijing, where the uniaxial compression and Brazilian tests are conducted. The loading rates are 0.5–1.0 MPa/s for the uniaxial compression test and 0.1–0.3 MPa/s for the Brazilian test. The triaxial compression tests are carried out by using the MTS-810 testing machine at the University of Minnesota, USA. The tests are controlled by a ring extensometer with a loading rate of 0.0005 mm/s. The confining pressures are 5 MPa, 10 MPa, 20 MPa, 30 MPa, 40 MPa, and 50 MPa. Eighteen specimens are divided into 6 groups for the uniaxial compression tests. The groupings and numbers of specimens for the Brazilian tests and triaxial compression tests are the same as those for the uniaxial compression tests.

The crack initiation stress and crack damage stress are two important parameters indicating the strength of rock based on the stress-strain response curve [29]. The crack initiation stress of granite is defined as the stress when the sample starts to have a crack volume strain. The crack damage stress is defined as the stress when the volume strain changes from increasing to decreasing. According to the crack strain model [30, 31], the crack volume strain ε_{vc} is given as follows:

$$\varepsilon_{vc} = \varepsilon_v - \varepsilon_{ve}, \tag{1}$$

where ε_v and ε_{ve} are the total volume strain and elastic volume strain, respectively.

The elastic volume strain could be calculated as follows:

$$\varepsilon_{ve} = \frac{1-2v}{E}(\sigma_1 - \sigma_3), \tag{2}$$

where σ_1 is the axial stress, σ_3 is the lateral stress, E is the elastic modulus, and v is Poisson's ratio in the elastic stage.

The mechanical parameters of the granite obtained from the experimental tests are given in Table 2. The granite parameters are calibrated to make the results of the numerical tests and those of the experimental tests consistent.

4.2. Calibration of the Tensile Young's Modulus E_t. According to previous studies on the calibration of Young's modulus [32, 33, 34, 35] and experiments on minerals [1], the initial microparameters of the four minerals in the granite are as shown in Table 3. The initial parallel bond Young's modulus of the plagioclase ($\overline{E}_x^*$), potash feldspar ($\overline{E}_j^*$), quartz ($\overline{E}_s^*$), and biotite ($\overline{E}_h^*$) are 88.1 GPa, 96.8 GPa, 94.5 GPa, and 30 GPa, respectively. It should be mentioned that the value of bond Young's modulus of every mineral represents the contact modulus between two particles representing the same mineral. The bond Young's modulus between two different mineral particles is equal to the average value of them. The values of $\overline{E}_x^*$, $\overline{E}_j^*$, $\overline{E}_s^*$, and $\overline{E}_h^*$ are multiplied by five coefficients, i.e., 1.0, 0.8, 0.6, 0.4, and 0.2, while the other microparameters are kept constant; these are used as the input parameters for the Brazilian disc test. Figure 6 illustrates the axial stress-strain curves of the five

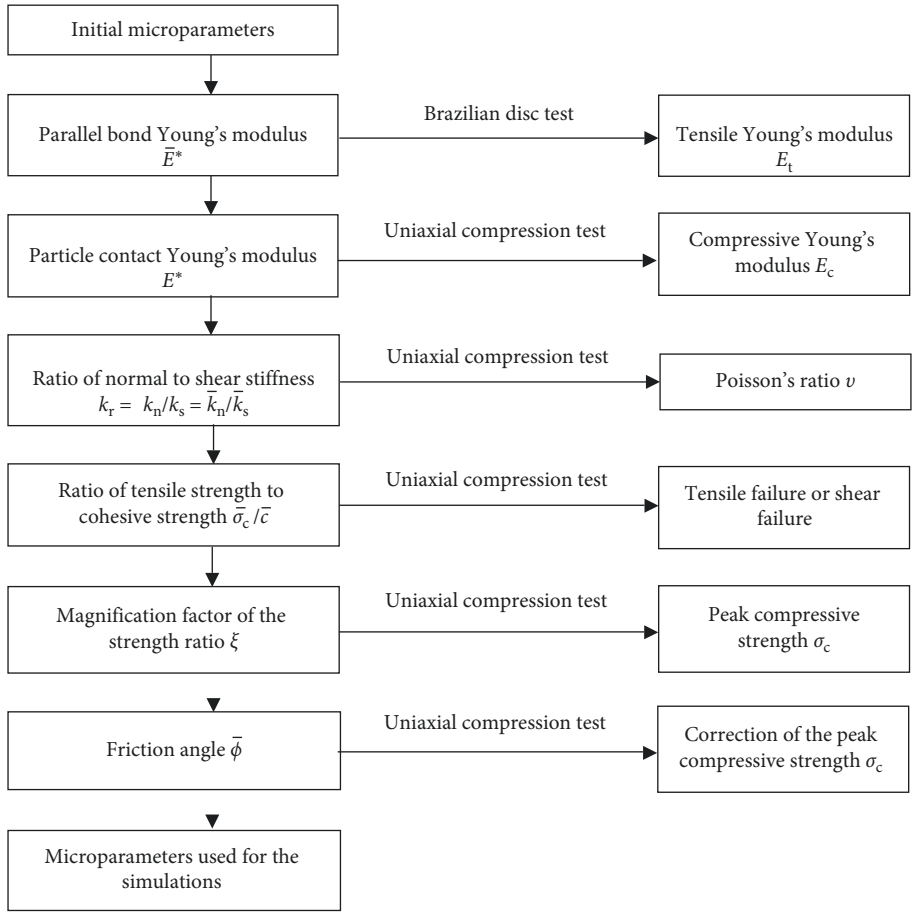

Figure 4: The calibration procedure and microparameters determination.

Brazilian tests. The numerical tensile Young's modulus can be measured based on the stress-strain curve. Furthermore, the relationship between the tensile Young's model and parallel bond Young's modulus of mineral particles can be obtained by using the linear fitting method, as illustrated in Figure 7 and equations (3)–(6):

$$\text{plagioclase: } \overline{E}_x^* = 3.38746E_t - 1.21061, \quad (3)$$

$$\text{potash feldspar: } \overline{E}_j^* = 3.72197E_t - 1.33016, \quad (4)$$

$$\text{quartz: } \overline{E}_s^* = 3.63354E_t - 1.29856, \quad (5)$$

$$\text{biotite: } \overline{E}_h^* = 1.1535E_t - 0.41224. \quad (6)$$

The experimental tensile Young's modulus of the granite is 40.99 GPa. Substituting that value into equations (3)–(6), the parallel bond Young's modulus of the plagioclase, potash feldspar, quartz, and biotite are calculated to be 137.64 GPa, 151.23 GPa, 147.64 GPa, and 46.86 GPa, respectively.

4.3. Calibration of the Compressive Young's Modulus E_c. The parallel bond Young's modulus of minerals is replaced with the values determined above. Then, the particle contact Young's modulus for different minerals is used to calibrate the compressive Young's modulus of the granite. Similar to the calibration of the tensile Young's modulus, the initial values of the particle contact Young's modulus of the four minerals are multiplied by five coefficients, i.e., 1.0, 0.8, 0.6, 0.4, and 0.2, while the other microparameters are held constant. Figure 8 shows the axial stress-strain curves from the five uniaxial compression tests. The relationships between the compressive Young's modulus and particle contact Young's modulus of every mineral are shown in Figure 9 and expressed as follows:

$$\text{plagioclase: } E_x^* = 2.25526E_c - 2.77281, \quad (7)$$

$$\text{potash feldspar: } E_j^* = 2.47798E_c - 3.05077, \quad (8)$$

$$\text{quartz: } E_s^* = 2.4191E_c - 2.97424, \quad (9)$$

$$\text{biotite: } E_h^* = 0.76797E_c - 0.9442. \quad (10)$$

By substituting the experimental compressive Young's modulus of 43.98 GPa into equations (7)–(10), the following values of the particle contact Young's modulus of the plagioclase, potassium feldspar, quartz, and biotite can be obtained: 96.41 GPa, 105.93 GPa, 103.42 GPa, and 32.83 GPa, respectively.

(a) (b)

Figure 5: Mechanical test equipment: (a) uniaxial compression test and Brazilian disc test (WEP-600); (b) triaxial compression test (MTS-810).

Table 2: Mechanical properties of Sanshandao granite from experiments.

Property	Density ($kg \cdot m^{-3}$)	Tensile strength (MPa)	Tensile Young's modulus (GPa)	Uniaxial compressive strength (MPa)	Comprehensive Young's modulus (GPa)	TS/UCS	Crack initiation (MPa)	Crack damage (MPa)	Poisson's ratio	Friction angle (°)	Cohesion (MPa)
Value	2686	12.40	40.99	94.37	43.98	0.13	37.75	81.16	0.20	49.96	17.19

Table 3: Initial values of the microparameters.

Microparameter	Plagioclase	Potash feldspar	Quartz	Biotite
$\overline{E}^*$	$\overline{E}_x^* = 88.1$ GPa	$\overline{E}_j^* = 96.8$ GPa	$\overline{E}_s^* = 94.5$ GPa	$\overline{E}_h^* = 30$ GPa
E^*	$E_x^* = 88.1$ GPa	$E_j^* = 96.8$ GPa	$E_s^* = 94.5$ GPa	$E_h^* = 30$ GPa
k_n/k_s	1	1	1	1
$\overline{k}_n/\overline{k}_s$	1	1	1	1
$\overline{\sigma}_c$	400 MPa	450 MPa	420 MPa	350 MPa
$\overline{c}$	800 MPa	900 MPa	840 MPa	700 MPa
$\overline{\phi}$	25°	30°	27°	20°
μ	0.5	0.5	0.5	0.5
$\overline{\lambda}$	1	1	1	1

4.4. Calibration of Poisson's Ratio v. The ratio of particle normal-to-shear stiffness and the ratio of parallel bond normal-to-shear stiffness affect Poisson's ratio of the model. Referring to previous research [33], the two ratios are considered to have the same value (i.e., $k_r = k_n/k_s = \overline{k}_n/\overline{k}_s$). In addition, the difference in the stiffness ratio for different minerals is ignored. The value of the stiffness ratio is multiplied by five coefficients (0.5, 1.0, 1.5, 2.0, and 2.5), while the other microparameters are held constant. The lateral and axial stress-strain curves from the uniaxial compression simulations are plotted in Figure 10, from which Poisson's ratio can be calculated. Furthermore, the relationship between the stiffness ratio and Poisson's ratio is obtained by linear fitting, as shown in Figure 11. The regression formula is expressed as follows:

$$v = 0.07643 + 0.09282k_r. \quad (11)$$

Poisson's ratio obtained from the uniaxial compressive tests is 0.20. By substituting it into equation (11), the particle stiffness ratio is determined to be 1.33.

4.5. Calibration of the Failure Mode. The failure mode of numerical samples is known to be controlled by the ratio of bond TS to bond cohesive strength [20, 36, 37]. If the value of $\overline{\sigma}_c/\overline{c}$ is small, the failure mode will be brittle. If the value of

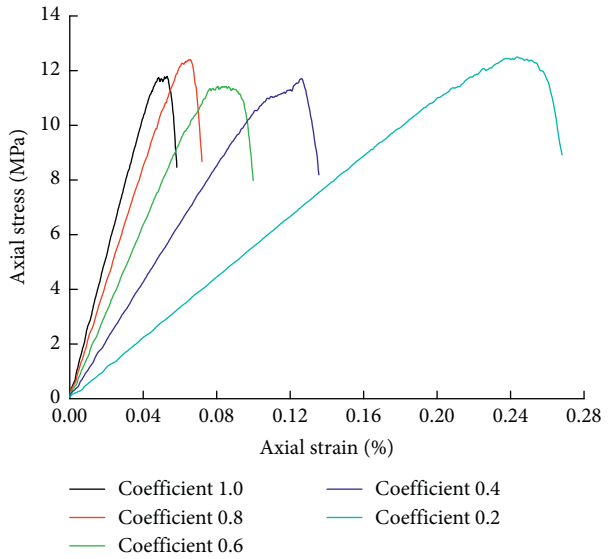

Figure 6: Axial stress-strain curves from Brazilian disc tests for the different coefficients of $\overline{E}^*$.

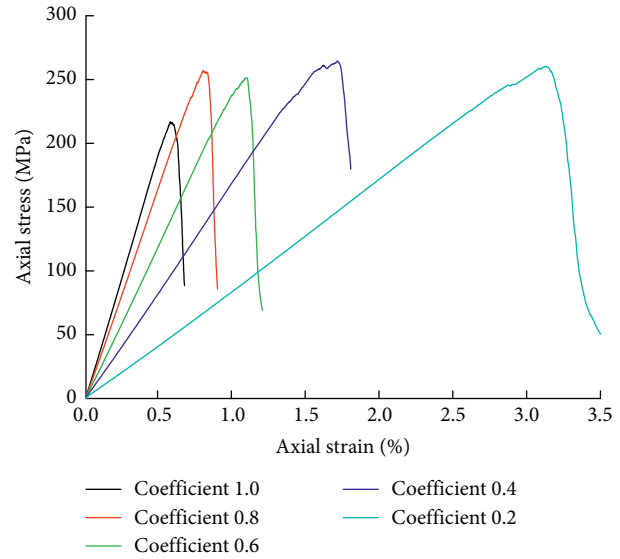

Figure 8: Axial stress-strain curves from uniaxial compression tests for the different coefficients of E^*.

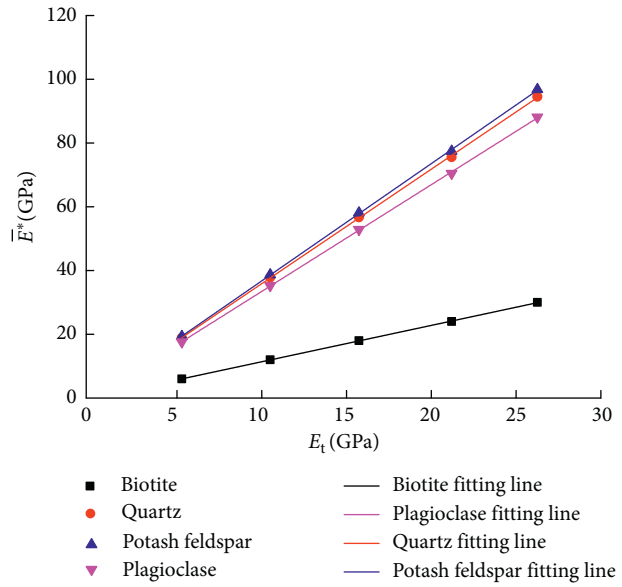

Figure 7: Relationships between the tensile Young's modulus and parallel bond Young's modulus of different minerals.

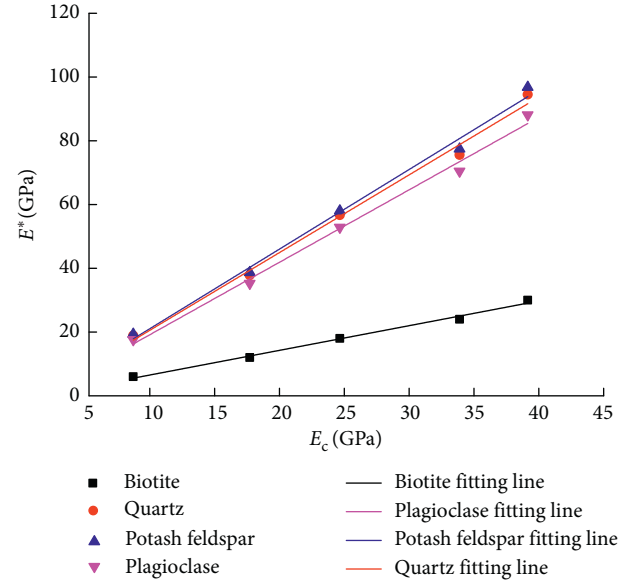

Figure 9: Relationships between the compressive Young's modulus and particle contact Young's modulus of different minerals.

$\overline{\sigma}_c/\overline{c}$ is large, ductile failure will occur in the simulations. The ratio of bond TS to bond cohesive strength is considered to be the same for different mineral components. Based on the microparameters determined above, the initial value of $\overline{\sigma}_c/\overline{c}$ is multiplied by five coefficients (0.5, 1.0, 1.2, 1.5, and 2.0). The number of microcracks and the failure pattern under different values of $\overline{\sigma}_c/\overline{c}$ are illustrated in Figure 12. Clearly, when the ratio of bond TS to bond cohesive strength is 0.5, the microcracks are almost all tensile cracks. When the ratio is larger than 1.0, shear microcracks appear first. Moreover, the larger the ratio is, the more the shear cracks dominate. The experimental results indicate that the failure of the granite under the uniaxial compression test involves both tensile and shear fractures but is dominated by tensile cracks. Therefore, the ratio of bond TS to bond cohesive strength is determined to be 1.0.

4.6. Calibration of the Uniaxial Compressive Strength. The initial parallel TS of the plagioclase, potash feldspar, quartz, and biotite is 400 MPa, 450 MPa, 420 MPa, and 350 MPa, respectively. A factor ξ is introduced as the coefficient of parallel TS, which is set to 0.25, 0.5, 1.0, 1.5, and 2.0. Five uniaxial compression tests are carried out based on the determined microparameters and the five different parallel TS values. Figure 13 shows the axial stress-strain curves under different coefficients ξ. Clearly, the larger the parallel

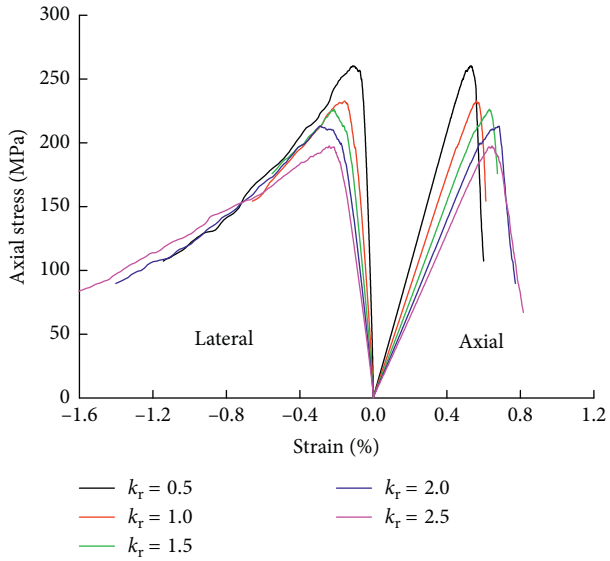

Figure 10: Stress-strain curves from uniaxial compression tests for the different stiffness ratios.

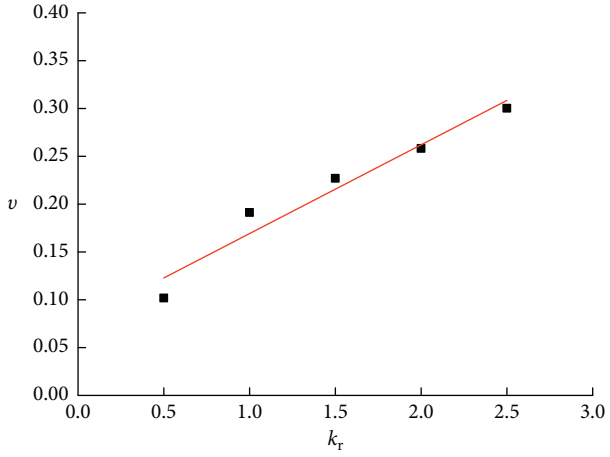

Figure 11: The relationship between Poisson's ratio and the stiffness ratio.

strength is, the larger the UCS is. The relationship between UCS and the coefficient ξ is illustrated in Figure 14. By linear fitting, the function is expressed as follows:

$$\sigma_c = 7.65488 + 160.24488\xi. \quad (12)$$

By substituting the experimental UCS of 94.37 MPa into equation (12), ξ is calculated to be 0.54. Furthermore, the parallel TS of each mineral can be obtained by multiplying the initial value by 0.54.

4.7. Calibration of the Friction Angle. Based on previous studies [35]; the initial friction angles of the plagioclase, potash feldspar, quartz, and biotite are determined to be 25°, 30°, 27°, and 20°, respectively. The friction angles of the minerals are multiplied by the coefficients of 0.25, 0.5, 1.0, 1.5, and 2.0, while the other microparameters are held constant. Figure 15 shows the axial stress-strain curves from the uniaxial compression tests for different friction angles. Clearly, the friction angle of minerals has no effect on the mechanical behavior of rock before reaching peak strength. In addition, the effect of the particle friction angle on postpeak behavior is little. Therefore, the friction angle coefficient is set to 0.5.

4.8. Results and Verification. The final microparameters obtained after performing calibration are given in Table 4. The microparameters are used for the Brazilian test and compression test. The tensile strength in the simulations is determined by the stress-strain curve. The tensile strength of the bonds $\overline{\sigma}_c$ was calibrated by matching the tensile strength of the rock σ_t obtained from direct tensile tests. The mineral of strength from high to low is potash feldspar, quartz, plagioclase, and biotite. The parameters for the biotite are significantly smaller than those for other minerals. It can be found in the simulations that the crack initiation is prone to occur at the points between the biotite particles or contact biotite particles. The crack initiation and postpeak response of the granite are mainly controlled by the heterogeneous microstructure [7]. Therefore, the multicomponent particle model could reproduce a more realistic mechanical behavior of the granite. Figure 16 shows the failure modes and axial stress-strain curves from the Brazilian experiment and numerical simulation. Clearly, the failure behaviors of the granite sample from the numerical simulation and the experiment are in good agreement. Notably, a brittle failure occurs in the experiments; thus, the stress-strain curve after the peak cannot be captured. Figure 17 illustrates the failure modes and stress-strain curves from the uniaxial compressive experiment and numerical simulation. According to the numerical results, the axial stress-strain curves before the peak are consistent with those of the experiments. Moreover, the failure patterns from the experiment and the numerical simulation are quite similar. Figure 18 shows the axial stress-strain curve and volumetric-axial strain curve from the simulations, which can be used to calculate the crack initial stress and crack damage stress. According to the crack strain model and equations (1) and (2), the crack initial stress and crack damage stress from the simulation (Figure 18) are approximately 36% of the UCS (34.66 MPa) and 89% of the UCS (85.72 MPa), respectively.

The comparison between the simulation results and experimental results on the basic macromechanical parameters is shown in Table 5. As shown, the errors of the tensile and compressive Young's moduli are 1.61% and 2.83%, respectively. The value of TS/UCS from the simulations is 0.12, which is 7.7% higher than that observed in the experiments. The numerical friction angle is just 0.5% larger than the experimental value. Clearly, the properties obtained from the simulations are in very good agreement with those from the experiments.

5. Triaxial Compression Tests and Discussion

The microparameters determined are used to simulate the mechanical behavior of samples under triaxial compressive

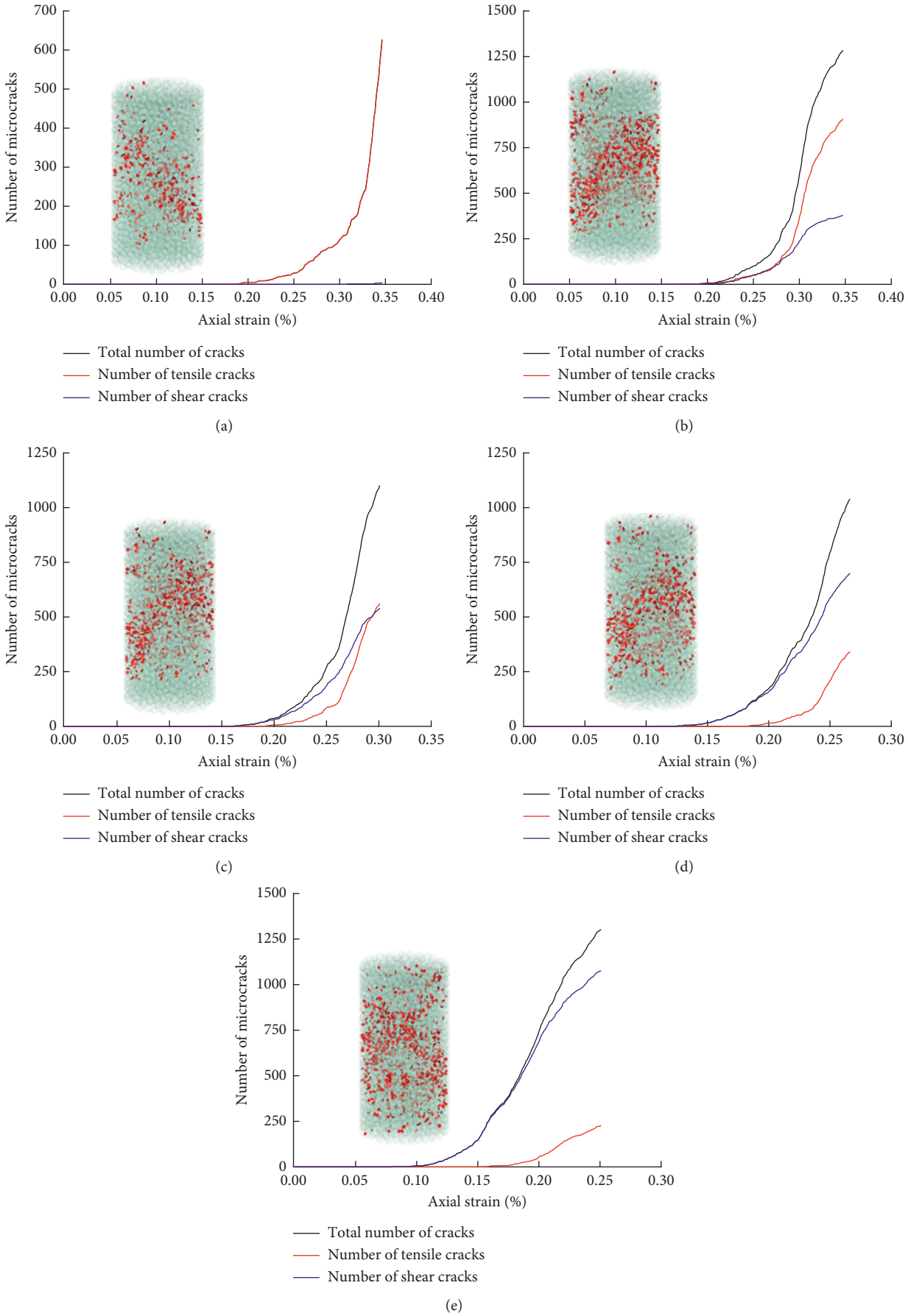

Figure 12: Microcrack number developments and failure pattern under different values of $\overline{\sigma}_c/\overline{c}$: (a) 0.5, (b) 1.0, (c) 1.2, (d) 1.5, and (e) 2.0.

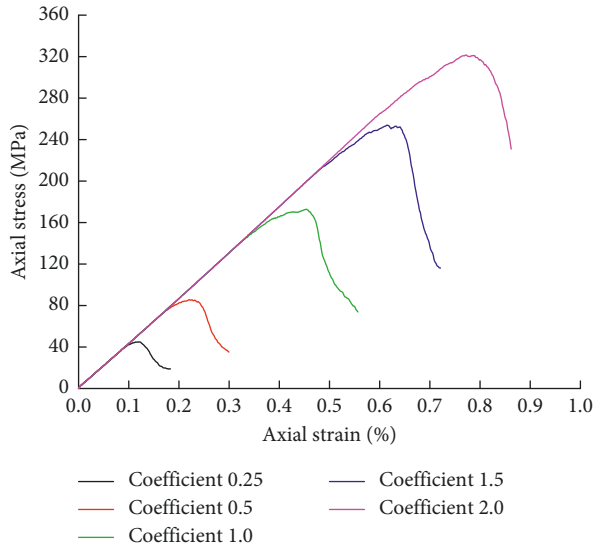

Figure 13: Axial stress-strain curves from uniaxial compression tests for the different coefficients of ξ.

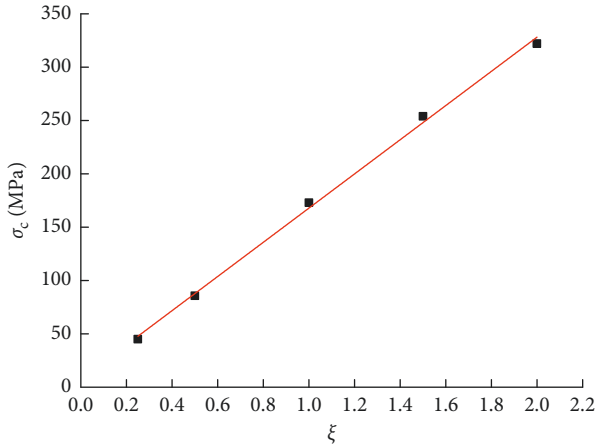

Figure 14: The relationship between the compressive strength and the strength coefficient ξ.

tests. The confining pressures are set to 5 MPa, 10 MPa, 20 MPa, 30 MPa, 40 MPa, and 50 MPa for the simulations and experiments. The axial stress-strain curves from the experiments and simulations are illustrated in Figure 19. As shown, the larger the confining pressure is, the larger the peak strength is. The stress-strain curves from the simulations before the peak stress is reached are in good agreement with those from the experiments. Because of the brittle or quasibrittle failure and the loading procedure and data capture procedure used in the experiments, the experimental curves after reaching the peak strength are more volatile than those of the simulations.

Using the Mohr–Coulomb failure criterion, the strength envelope curves of the experiments and simulations are obtained, as shown in Figure 20. Clearly, when the confining pressure is in the range of 0–50 MPa, the strength envelope curves are almost linear, and the regression equations are as follows:

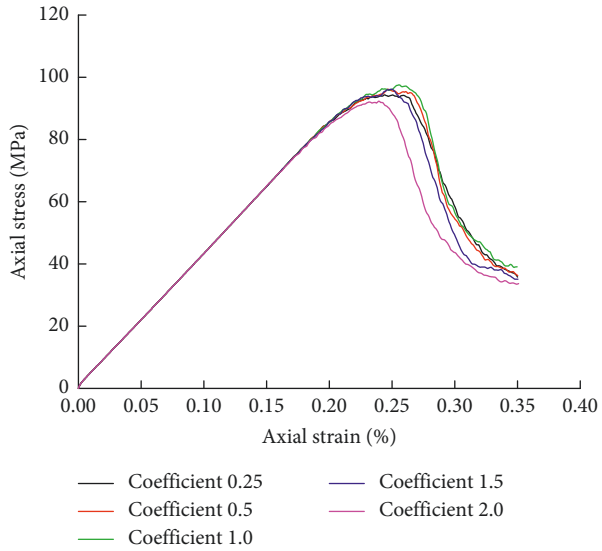

Figure 15: Axial stress-strain curves from uniaxial compression tests for the different coefficients of the friction angle.

$$\begin{aligned} &\text{experiment: } \sigma_1 = 7.53116\sigma_3 + 112.30462, \\ &\text{simulation: } \sigma_1 = 7.63534\sigma_3 + 113.04038. \end{aligned} \tag{13}$$

It is important to compare the simulations results with the experimental results based on the parameters of the HB failure criterion. Most previous studies could not calibrate the strength parameter of the HB failure criterion. The HB failure criterion is expressed as follows [38, 39]:

$$\sigma_1 = \sigma_3 + \sigma_c\left(m_i\frac{\sigma_3}{\sigma_c} + s\right)^{\alpha}, \tag{14}$$

where m_i is the parameter accounting for the rock hardness; s is the measure of how fractured the rock is; and α reflects the system's bias.

The fitting equations obtained from the experiments and simulations are given in equations (15) and (16), respectively. Figure 21 presents the strength envelope curves obtained from the experiments and simulations, which are in good agreement. Clearly, the m_i parameter from the simulations is 17% smaller than that from the experiments:

$$\sigma_1 = \sigma_3 + 74.03808\left(10.91621\frac{\sigma_3}{74.03808} + 1.32708\right)^{0.79835}, \tag{15}$$

$$\sigma_1 = \sigma_3 + 96.7697\left(9.02805\frac{\sigma_3}{96.7697} + 1.14264\right)^{0.86144}. \tag{16}$$

6. Conclusions

In this paper, we proposed a new three-dimensional MBPM for heterogeneous rocks. The models, consisting of four mineral components, were built based on a microscopic analysis of Sanshandao granite. The cylindrical and disc models were built to simulate the behavior of Sanshandao

Table 4: Microparameters of the multicomponent bonded-particle model after performing calibration.

Mineral	R_{min} (mm)	R_{max}/R_{min}	ρ (kg·m^{-3})	μ	E^* (GPa)	k_r	$\overline{E}^*$ (GPa)	$\overline{\lambda}$	n	$\overline{\sigma}_c$ (MPa)	$\overline{c}$ (MPa)	$\overline{\phi}$ (°)
Plagioclase	1.5	1.66	2560	0.5	96.41	1.33	137.64	1	0.36	224	224	12.5
Potash feldspar	1.5	1.66	2630	0.5	105.93	1.33	151.23	1	0.36	252	252	15.0
Quartz	1.5	1.66	2650	0.5	103.42	1.33	147.64	1	0.36	235.2	235.2	13.5
Biotite	1.5	1.66	3050	0.5	32.83	1.33	46.86	1	0.36	196	196	10

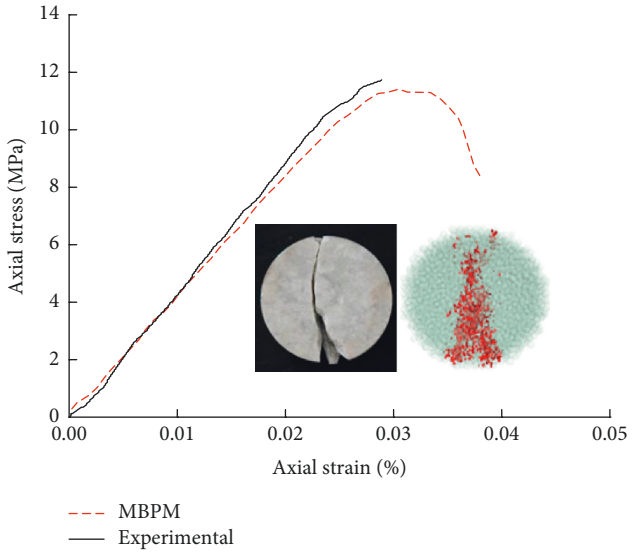

Figure 16: Comparison of experimental results and numerical results on the Brazilian disc test.

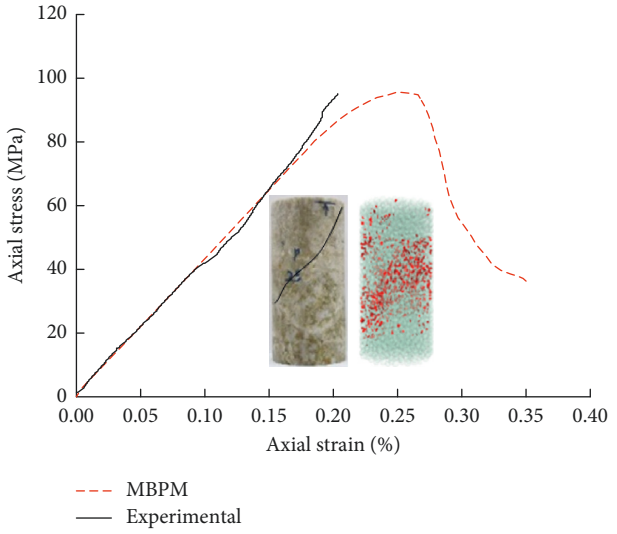

Figure 17: Comparison of experimental results and numerical results on the uniaxial compression test.

granite under uniaxial and triaxial compression tests and Brazilian disc tests. To improve the efficiency of calibration, a new method for determining the microparameters of the minerals was proposed. The uniaxial compression, triaxial compression, and Brazilian tests were carried out in the lab. By using the linear fitting method, the microparameters were

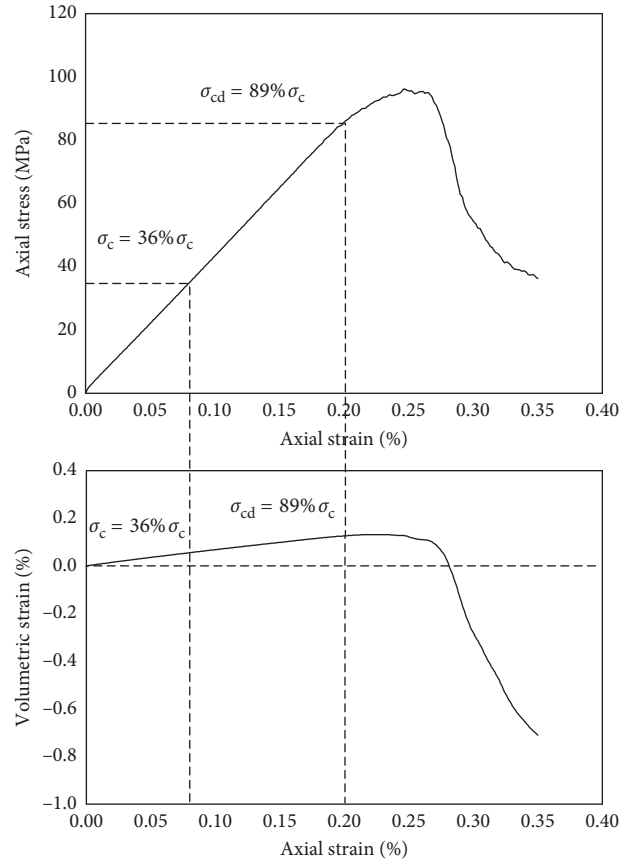

Figure 18: Axial stress-strain curve and volumetric-axial strain curve from the numerical uniaxial compression test.

Table 5: Comparison of mechanical properties of the Sanshandao granite from the experimental and numerical results.

Mechanical properties	Experimental result	Numerical result	Error (%)
E_c (GPa)	43.98	43.27	1.61
E_t (GPa)	40.99	42.15	2.83
υ	0.2	0.18	10.00
σ_{ci} (MPa)	37.75	34.66	8.20
σ_{cd} (MPa)	81.16	85.72	5.62
σ_c (MPa)	94.37	96.16	1.90
σ_t (MPa)	12.40	11.40	8.06
TS/UCS	0.13	0.12	7.7
C (MPa)	17.19	17.40	1.22
φ (°)	49.96	50.21	0.50

determined quickly and accurately. After the calibrations, the multicomponent particle model well reproduced the macrobehavior of the rock. The findings of our study are as follows:

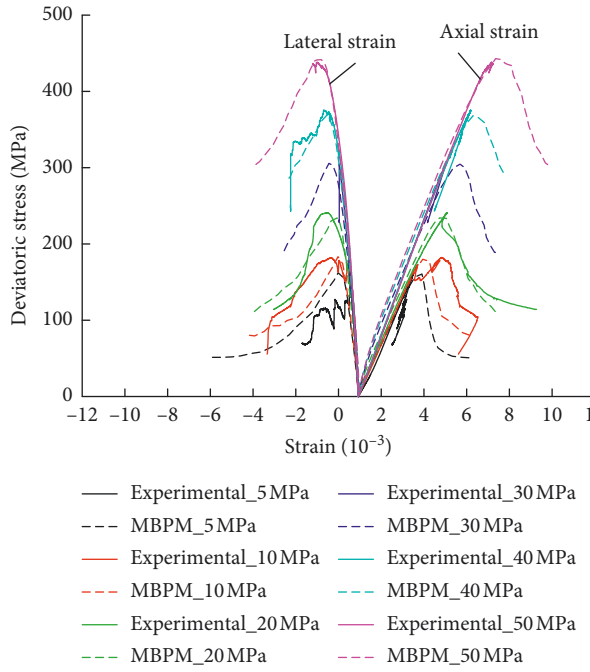

Figure 19: Comparisons of deviatoric stress-strain curves from the experimental results and numerical results of triaxial compression tests.

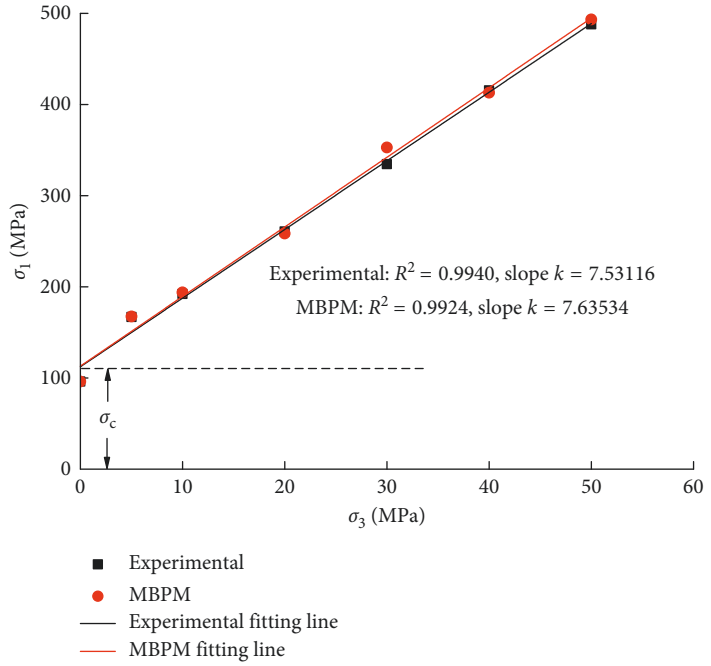

Figure 20: Mohr–Coulomb strength envelopes from experimental results and numerical results.

(1) The MBPM becomes a linear contact model after cementation failure. The parallel bond parameters affect the behaviors under both tension and compression, while the particle contact parameters affect only the compressive behavior. Therefore, a positive correlation exists between the particle contact Young's modulus and compressive Young's modulus of rocks.

(2) The ratio of bond TS to bond cohesive strength greatly affects the failure mode and crack evolution under compression. When the ratio is larger than 1.0, shear microcracks appear first. Moreover, the larger the ratio is, the more dominant the shear cracks are. The friction angle of minerals has no effect on the mechanical behavior of rock before the peak strength

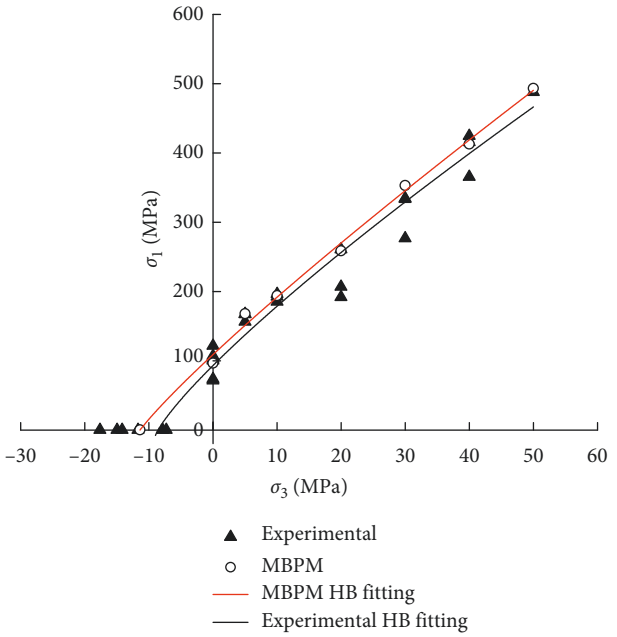

Figure 21: Hoek–Brown strength envelopes from experimental results and numerical results.

is reached. In addition, the effect of the particle friction angle on postpeak behavior is little.

(3) The Mohr–Coulomb and HB strength envelopes from the numerical results are in good agreement with those from the experiments. The value of TS/UCS from the simulations is 0.12, which is 7.7% higher than that from the experiments. The numerical friction angle is just 0.5% larger than the experimental value. In addition, the m_i parameter from the simulations is 17% smaller than that from the experiments. The MBPM significantly improves the accuracy of the above three parameters, and the linear fitting calibration method provides a fast and efficient way to determine the microparameters of particles for heterogeneous rocks.

Symbols

$\overline{E}^*$: Parallel bond Young's modulus (GPa)
$\overline{E}_x^*$: Parallel bond Young's modulus of plagioclase (GPa)
$\overline{E}_j^*$: Parallel bond Young's modulus of potash feldspar (GPa)
$\overline{E}_s^*$: Parallel bond Young's modulus of quartz (GPa)
$\overline{E}_h^*$: Parallel bond Young's modulus of biotite (GPa)
E^*: Particle contact Young's modulus (GPa)
E_x^*: Particle contact Young's modulus of plagioclase (GPa)
E_j^*: Particle contact Young's modulus of potash feldspar (GPa)
E_s^*: Particle contact Young's modulus of quartz (GPa)
E_h^*: Particle contact Young's modulus of biotite (GPa)
$\underline{k}_n/\underline{k}_s$: Ratio of particle normal-to-shear stiffness
$\overline{k}_n/\overline{k}_s$: Ratio of parallel bond normal-to-shear stiffness
k_r: Ratio of normal stiffness to shear stiffness
$\overline{\sigma}_c$: Parallel bond tensile strength (MPa)
$\overline{c}$: Parallel bond cohesion (MPa)
$\overline{\phi}$: Friction angle of particles (°)
$\underline{\mu}$: Friction coefficient of particles
$\overline{\lambda}$: Radius multiplier
ξ: Magnification factor of the strength ratio
R_{min}: Minimum particle radius (mm)
R_{max}/R_{min}: Particle size ratio
ρ: Particle bulk density (kg·m^{-3})
ρ_g: Rock density (kg·m^{-3})
n: Porosity
σ_t: Tensile strength (TS) (MPa)
E_t: TS Young's modulus (GPa)
σ_c: Uniaxial compressive strength (UCS) (MPa)
E_c: UCS Young's modulus (GPa)
σ_{ci}: Crack initiation (MPa)
σ_{cd}: Crack damage (MPa)
υ: Poisson's ratio of rock
φ: Friction angle of rock (°)
C: Cohesion of rock (MPa)
σ_1: Axial stress (MPa)
σ_3: Lateral stress (MPa)
R^2: Correlation coefficient
k: Slope
m_i: Parameter accounting for rock hardness
s: Measure of how fractured the rock is
α: Reflection of system bias
E: Elastic modulus (GPa)
ε_{vc}: Crack volume strain (%)
ε_v: Total volume strain (%)
ε_{ve}: Elastic volume strain (%).

Data Availability

The data of this study are available from the corresponding author upon request.

Conflicts of Interest

The authors declare that they have no conflicts of interest.

Acknowledgments

This study was funded by the National Key R&D Plan of China (nos. 2018YFE0101100 and 2018YFC0808403) and National Natural Science Foundation of China (no. 51774022).

References

[1] K. Farahmand and M. S. Diederichs, "A calibrated synthetic Rock Mass (SRM) model for simulating crack growth in granitic rock considering grain scale heterogeneity of polycrystalline rock," in *Proceedings of 49th US Rock Mechanics/Geomechanics Symposium*, American Rock Mechanics Association, San Francisco, CA, USA, June-July 2015.

[2] R. L. Kranz, "Microcracks in rocks: a review," *Tectonophysics*, vol. 100, no. 1–3, pp. 449–480, 1983.

[3] J. Arzúa and L. R. Alejano, "Dilation in granite during servo-controlled triaxial strength tests," *International Journal of Rock Mechanics and Mining Sciences*, vol. 61, pp. 43–56, 2013.

[4] F. Rummel and C. Fairhurst, "Determination of the post-failure behavior of brittle rock using a servo-controlled testing machine," *Rock Mechanics*, vol. 2, no. 4, pp. 189–204, 1970.

[5] U. W. Vogler and K. Kovári, "Suggested methods for determining the strength of rock materials in triaxial compression," *International Journal of Rock Mechanics and Mining Sciences*, vol. 15, pp. 47–51, 1978.

[6] J. Wang, Z. Wang, and S. Yang, "A coupled macro- and meso-mechanical model for heterogeneous coal," *International Journal of Rock Mechanics and Mining Sciences*, vol. 94, pp. 64–81, 2017.

[7] H. Lan, C. D. Martin, and B. Hu, "Effect of heterogeneity of brittle rock on micromechanical extensile behavior during compression loading," *Journal of Geophysical Research*, vol. 115, no. B1, article B01202, 2010.

[8] D. O. Potyondy, P. A. Cundall, and C. A. Lee, "Modeling rock using bonded assemblies of circular particles," in *Proceedings of 2nd North American Rock Mechanics symposium*, pp. 1937–1944, American Rock Mechanics Association, Montreal, Canada, June 1996.

[9] A. Fakhimi, F. Carvalho, T. Ishida, and J. F. Labuz, "Simulation of failure around a circular opening in rock," *International Journal of Rock Mechanics and Mining Sciences*, vol. 39, no. 4, pp. 507–515, 2002.

[10] X.-P. Zhang and L. N. Y. Wong, "Cracking processes in rock-like material containing a single flaw under uniaxial compression: a numerical study based on parallel bonded-particle model approach," *Rock Mechanics and Rock Engineering*, vol. 45, pp. 711–737, 2012.

[11] X.-P. Zhang and L. N. Y. Wong, "Crack initiation, propagation and coalescence in rock-like material containing two flaws: a numerical study based on bonded-particle model approach," *Rock Mechanics and Rock Engineering*, vol. 46, no. 5, pp. 1001–1021, 2013.

[12] X.-P. Zhang and L. N. Y. Wong, "Loading rate effects on cracking behavior of flaw-contained specimens under uniaxial compression," *International Journal of Fracture*, vol. 180, no. 1, pp. 93–110, 2013.

[13] X.-P. Zhang, Q. Zhang, and S. Wu, "Acoustic emission characteristics of the rock-like material containing a single flaw under different compressive loading rates," *Computers and Geotechnics*, vol. 83, pp. 83–97, 2017.

[14] P.-Q. Ji, X.-P. Zhang, and Q. Zhang, "A new method to model the non-linear crack closure behavior of rocks under uniaxial compression," *International Journal of Rock Mechanics and Mining Sciences*, vol. 112, pp. 171–183, 2018.

[15] P. H. S. W. Kulatilake, B. Malama, and J. Wang, "Physical and particle flow modeling of jointed rock block behavior under uniaxial loading," *International Journal of Rock Mechanics and Mining Sciences*, vol. 38, no. 5, pp. 641–657, 2001.

[16] J.-W. Park and J.-J. Song, "Numerical simulation of a direct shear test on a rock joint using a bonded-particle model," *International Journal of Rock Mechanics and Mining Sciences*, vol. 46, no. 8, pp. 1315–1328, 2009.

[17] B. A. Poulsen and D. P. Adhikary, "A numerical study of the scale effect in coal strength," *International Journal of Rock Mechanics and Mining Sciences*, vol. 63, pp. 62–71, 2013.

[18] Y. Zhou, S. H. Wu, J. J. Jiao, and X. P. Zhang, "Research on mesomechanical parameters of rock and soil mass based on BP neural network," *Rock and Soil Mechanics*, vol. 32, pp. 3821–3826, 2011, in Chinese.

[19] F. Y. Liu, P. Y. Chen, and H. M. Yu, "PFC simulation of uniaxial compression and Brazilian splitting test of rock based on flat-jointed bonded-particle material," *Journal of Yangtze River Scientific Research Institute*, vol. 33, pp. 60–65, 2016, in Chinese.

[20] S. Wu and X. Xu, "A study of three intrinsic problems of the classic discrete element method using flat-joint model," *Rock Mechanics and Rock Engineering*, vol. 49, no. 5, pp. 1813–1830, 2016.

[21] J. A. Vallejos, J. M. Salinas, A. Delonca, and D. M. Ivars, "Calibration and verification of two bonded-particle models for simulation of intact rock behavior," *International Journal of Geomechanics*, vol. 17, no. 4, pp. 1–11, 2016.

[22] J. A. Vallejos, K. Suzuki, A. Brzovic, and D. M. Ivars, "Application of synthetic rock mass modeling to veined core-size samples," *International Journal of Rock Mechanics and Mining Sciences*, vol. 81, pp. 47–61, 2016.

[23] C. E. Fairhurst and J. A. Hudson, "Draft ISRM suggested method for the complete stress-strain curve for intact rock in uniaxial compression," *International Journal of Rock Mechanics and Mining Sciences*, vol. 36, pp. 279–289, 1999.

[24] X.-P. Zhang and L. N. Y. Wong, "Choosing a proper loading rate for bonded-particle model of intact rock," *International Journal of Fracture*, vol. 189, no. 2, pp. 163–179, 2014.

[25] D. M. Ivars, M. E. Pierce, C. Darcel et al., "The synthetic rock mass approach for jointed rock mass modelling," *International Journal of Rock Mechanics and Mining Sciences*, vol. 48, no. 2, pp. 219–244, 2011.

[26] Y. Wang and F. Tonon, "Modeling Lac du Bonnet granite using a discrete element model," *International Journal of Rock Mechanics and Mining Sciences*, vol. 46, no. 7, pp. 1124–1135, 2009.

[27] B. Yang, Y. Jiao, and S. Lei, "A study on the effects of microparameters on macroproperties for specimens created by bonded particles," *Engineering Computations*, vol. 23, no. 6, pp. 607–631, 2006.

[28] J. Yoon, "Application of experimental design and optimization to PFC model calibration in uniaxial compression simulation," *International Journal of Rock Mechanics and Mining Sciences*, vol. 44, no. 6, pp. 871–889, 2007.

[29] L. Xue, S. Qin, Q. Sun, Y. Wang, L. M. Lee, and W. Li, "A study on crack damage stress thresholds of different rock types based on uniaxial compression tests," *Rock Mechanics and Rock Engineering*, vol. 47, no. 4, pp. 1183–1195, 2014.

[30] C. D. Martin, "Seventeenth Canadian geotechnical colloquium: the effect of cohesion loss and stress path on brittle rock strength," *Canadian Geotechnical Journal*, vol. 34, no. 5, pp. 698–725, 1997.

[31] C. D. Martin and N. A. Chandler, "The progressive fracture of Lac du Bonnet granite," *International Journal of Rock Mechanics and Mining Sciences & Geomechanics Abstracts*, vol. 31, no. 6, pp. 643–659, 1994.

[32] O. K. Mahabadi, A. Lisjak, A. Munjiza, and G. Grasselli, "Y-Geo: new combined finite-discrete element numerical code for geomechanical applications," *International Journal of Geomechanics*, vol. 12, no. 6, pp. 676–688, 2012.

[33] D. O. Potyondy, "Simulating stress corrosion with a bonded-particle model for rock," *International Journal of Rock Mechanics and Mining Sciences*, vol. 44, no. 5, pp. 677–691, 2007.

[34] D. O. Potyondy and P. A. Cundall, "A bonded-particle model for rock," *International Journal of Rock Mechanics and Mining Sciences*, vol. 41, no. 8, pp. 1329–1364, 2004.

[35] Y. Zhou, Y. T. Gao, S.-C. Wu et al., "An equivalent crystal model for mesoscopic behaviour of Rock," *Chinese Journal of Rock Mechanics and Engineering*, vol. 34, pp. 511–519, 2015, in Chinese.

[36] X. Ding and L. Zhang, "A new contact model to improve the simulated ratio of unconfined compressive strength to tensile strength in bonded particle models," *International Journal of Rock Mechanics and Mining Sciences*, vol. 69, pp. 111–119, 2014.

[37] L. Scholtès and F.-V. Donzé, "A DEM model for soft and hard rocks: role of grain interlocking on strength," *Journal of the Mechanics and Physics of Solids*, vol. 61, no. 2, pp. 352–369, 2013.

[38] E. Eberhardt, "The Hoek–Brown failure criterion," *Rock Mechanics and Rock Engineering*, vol. 45, no. 6, pp. 981–988, 2012.

[39] X.-P. Zhang, Q. Liu, S. Wu, and X. Tang, "Crack coalescence between two non-parallel flaws in rock-like material under uniaxial compression," *Engineering Geology*, vol. 199, pp. 74–90, 2015.